sciendo

Green Sciences, 27, 3, 1—9, 10.2478/pjct-2025-0012

Fluorescent Polysaccharide-Silica-Based Drug Conjugate Nanocarrier Inhibit Non-small Cell Lung Cancer Proliferation

Taixu Sun[1], Dengfeng Ge[1], Ying Zhang[2], Bin Zhang[2*]

[1]Nanjing University of Traditional Chinese Medicine, Nanjing, Jiangsu, China
[2]Department of cardiothoracic surgery, Jiangsu Provincial Hospital of Traditional Chinese Medicine, Nanjing, Jiangsu, China
[*]*Corresponding authors:* e-mail: drzhangbin@163.com

Non-small cell lung cancer (NSCLC) is a highly prevalent and aggressive type of lung cancer, often associated with a poor prognosis. Cucurbitacin B, a natural tetracyclic triterpene, has demonstrated remarkable anticancer activity. In this study, we engineered a novel drug delivery system, Dex-APDMS@CP1@1@Cucurbitacin B, which incorporates synthetically derived compound 1 to enhance the therapeutic efficacy of Cucurbitacin B. The system was comprehensively characterized using X-ray diffraction (XRD), scanning electron microscopy (SEM), thermogravimetric analysis (TGA), and nitrogen adsorption techniques. Results revealed excellent stability, a uniform particle size of approximately 500 nm, and a high drug-loading efficiency of 35.2 ± 2.1 wt%. Additionally, the in vitro drug release study indicated that 88.6 ± 3.5% of Cucurbitacin B was released within 12 hours, demonstrating a rapid release profile. The successful encapsulation of the drug was further confirmed by effective fluorescence quenching. In vitro experiments showed that the Dex-APDMS@CP1@1@Cucurbitacin B system significantly inhibited the proliferation of NSCLC cells, highlighting its great potential for targeted cancer therapy.

Keywords: NSCLC, Cucurbitacin B, Fluorescence quenching.

Received: 02 May 2025; Accepted: 26 June 2025; Available online: 20.10.2025.

INTRODUCTION

The design of novel drug delivery systems, particularly nanocarriers loaded with Cucurbitacin B, holds significant promise for enhancing the therapeutic efficacy of Cucurbitacin B in treating non-small cell lung cancer (NSCLC)[1–3]. NSCLC, which constitutes approximately 85% of all lung cancer cases, is known for its aggressive nature and potential metastasis to other organs[4]. Cucurbitacin B, a naturally occurring tetracyclic triterpene, demonstrates potent biological activities, including inhibition of tumor cell proliferation and induction of apoptosis, likely via interference with key signaling pathways such as JAK-STAT and Wnt/β-catenin[5, 6]. Its ability to modulate inflammatory responses and immune functions further emphasizes its potential as an effective anticancer agent[7, 8]. The development of efficient nanocarriers for Cucurbitacin B delivery could overcome challenges related to its bioavailability and enhance its therapeutic effects, offering a promising strategy for NSCLC treatment[9, 10].

Metal-organic frameworks (MOFs) are porous materials self-assembled from metal ions and organic ligands through coordination interactions, exhibiting high tunability and excellent chemical stability[11, 12]. Compared to porous organic polymers (POPs) and covalent organic frameworks (COFs), MOFs demonstrate superior chemical adsorption properties, making them highly applicable in catalysis, gas storage, and material separation[13, 14]. However, the rigid structure of many MOFs limits their flexibility in drug delivery, a critical feature for drug carriers[15].

Natural macromolecules, due to their excellent biocompatibility, low toxicity, and unique biological effects, offer distinct advantages over synthetic materials and have been widely applied in the preparation and modification of nanocarriers[16, 17]. As an important class of natural macromolecules, polysaccharides (such as chitosan (CS), hyaluronic acid (HA), dextran (Dex), and alginate (Alg)) have gained extensive research attention due to their abundance in nature and cost-effective processing advantages[18]. Taking Dex as an example, its excellent biodegradability and biocompatibility have led to widespread applications in pharmacology[19, 20]. The branched structure and numerous hydroxyl groups of Dex make it an ideal platform for chemical modification, enabling the attachment of various molecules (such as targeting ligands and drug molecules) to construct multifunctional carriers[21]. However, polysaccharide-based drug delivery systems (DDS) still face challenges, including the complexity of carrier material synthesis, higher in vivo toxicity, insufficient biodegradability, and shorter circulation times than expected[21]. To overcome these limitations, combining polysaccharide-modified polymer--silica materials with metal-organic frameworks (MOFs) to create new drug carrier systems can significantly improve the biocompatibility, stability, and targeting ability of drug carriers[22]. The superior porous structure and functionalization capabilities of MOFs offer unique advantages in drug delivery. Polysaccharide modification can further enhance their water solubility, biodegradability, and compatibility with biological systems, substantially improving therapeutic efficacy while effectively reducing nonspecific side effects, particularly in the treatment of diseases such as cancer[23, 24].

In this study, we successfully synthesized Dex--APDMS@CP1@1@Cucurbitacin B (Scheme 1), a novel fluorescence-based drug delivery system. To enhance the therapeutic efficacy of Cucurbitacin B against NSCLC. In this study, we developed a novel drug delivery system, Dex-APDMS@CP1@1@Cucurbitacin B, incorporating synthetically prepared compound 1, which significantly enhances the therapeutic efficacy of Cucurbitacin B. The combination of compound 1 and Cucurbitacin B creates

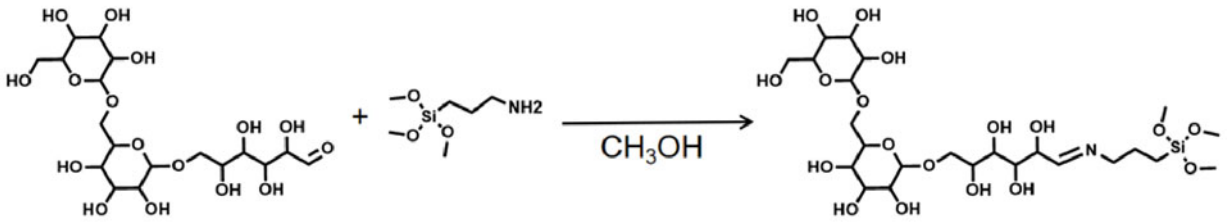

Scheme 1. The synthesis of Dex-APDMS

a synergistic effect, enhancing the therapeutic outcome by leveraging the unique properties of both compounds. This synergism results in improved efficacy in targeting and inhibiting NSCLC cell proliferation, thus offering a promising strategy for cancer treatment.

EXPERIMENTAL

Materials and instrumentation

The organic ligand and organic solvent are commercially available and used without further purification. Elemental analyses (C, H, and N) were performed on a Perkin-Elmer 2400 CHN elemental analyzer. Powder X-ray diffraction (PXRD) analysis was conducted on a max200PC diffractometer with Cu-Kα radiation (λ = 1.5418 Å). The thermostability of **1** was investigated via the thermogravimetric analysis experiment conducted on a NETSCHZ STA-449C thermoanalyzer under nitrogen atmosphere. The luminescent spectra were measured by a FLS920 luminescence spectrophotometer. UV–vis diffused reflectance spectrum for the solid samples of **1** was collected on a UV–vis spectrophotometer (UV-3600, Shimadzu, Japan) with a $BaSO_4$ plate as a reflectance standard (100% reflectance).

Synthesis of $[Cu(L)_{0.5}(CN)]_n$ (CP1) and compound 1

A mixture of CuCN (0.100 mmol), L (0.05 mmol), DMF (3.0 mL) and CH_3CN (1.0 mL) was put into a 25 mL Teflon-lined stainless steel vessel, which was further sealed and heated at 140 °C for 72 h. Brown block crystals of CP**1** were isolated in 32% yield based on CuCN Elemental analysis calcd. for $C_{11}H_6CuN_4O$ (273.75): C, 48.22; H, 2.19; N, 20.46%. Found: C, 48.24; H, 2.21; N, 20.37%.

Compound 1 was synthesized via a one-pot condensation of 1,3-cyclohexanedione (0.112 g, 1 mmol), methyl 3-aminocrotonate (0.115 g, 1 mmol), and 3,5-difluorobenzaldehyde (0.146 g, 1 mmol) in 10 mL of ethanol with two drops of acetic acid. The mixture was refluxed for 6–8 hours, and the reaction progress was monitored by TLC (ethyl acetate/hexane, 3:2). After solvent removal, the crude product was purified by column chromatography (ethyl acetate/hexane = 1:2) or recrystallization from ethanol to yield compound 1 (65%).

Table 1. The crystal data for CP1 and compound 1

Parameter	CP1	Compound 1
Formula	$C_{11}H_6CuN_4O$	$C_{18}H_{17}F_2NO_3$
Fw	273.75	333.33
Crystal system	monoclinic	Monoclinic
Space group	$P2_1/c$	$P2(1)/c$
a (Å)	9.684(2)	13.167(4)
b (Å)	5.2640(17)	8.399(3)
c (Å)	23.985(2)	14.294(5)
α°	90	90
β°	96.844(2)	92.952(6)
γ°	90	90
Volume (Å^3)	1214.0(5)	1578.6(9)
Z	4	4
$D_{calcd.}$[mg·m^{-3}]	1.498	1.402
Abs. coeff. (mm^{-1})	1.786	0.111
Total reflections	7119	7675
Unique reflections	2129	2776
Goodness of fit on F^2	1.073	1.071
Final *R* indices [*I*>2sigma(I^2)]	*R*=0.0350, wR_2= 0.0751	*R*=0.0805, wR_2= 01914
R (all data)	*R*=0.0450, wR_2= 0.0795	*R*=0.1076, wR_2= 0.2053

The crystal structure data of CP**1** and compound 1 were recorded on a computer-controlled Rigaku Mercury CCD diffractometer with the graphite-monochromated Mo-Kα radiation at room temperature. The structure was solved by direct methods and refined by full-matrix least squares via the Olex2 1.2 crystallographic software package. All non-hydrogen atoms were refined with anistropic thermal parameters, and all hydrogen atoms were fixed at their ideal positions. The crystallographica data and refinements of CP**1** and compound 1 are listed in Table 1.

Synthesis of Dex-APDMS@CP1@1@Cucurbitacin B

100 mg of Dextran (Dex) was dissolved in 30 mL of methanol. Next, 3-aminopropyltrimethoxysilane (APDMS) (0.2 mmol, 36.6 mg) was added to the mixture, and the reaction was allowed to proceed under reflux conditions for 24 hours. After completion of the reaction, the product was purified by dialysis and dried to obtain Dex-APDMS material.

Subsequently, CP1 (0.1 mmol) was mixed with Dex--APDMS in a suitable solvent, and the resulting mixture was stirred under controlled conditions for 12 hours. Following this step, Cucurbitacin B (5 mg) and compound 1 (5 mg) were incorporated into the composite material. Finally, Dex-APDMS@CP1@1@Cucurbitacin B was isolated after washing and freeze-drying, yielding the desired product for further characterization and use in drug delivery systems.

Loading and release of drugs

Precisely 200 mg of Dex-APDMS@CP1@1 nanocarriers were weighed and placed in a 50 mL clean conical flask, to which 5 mL of Cucurbitacin B DMSO solution at a concentration of 10 mg/mL was slowly added. The mixture was incubated in a constant-temperature shaker at 150 rpm for 24 hours at room temperature. After incubation, the sample was transferred to a 50 mL centrifuge tube and centrifuged at 12,000 rpm for 15 minutes. The supernatant was discarded, and the precipitate was collected to obtain the drug-loaded Dex-APDMS@CP1@1@Cucurbitacin B sample. The centrifuged supernatant was transferred to a 10 mL volumetric flask, diluted and made up to volume with DMSO, and mixed thoroughly. The concentration of Cucurbitacin B in the diluted solution was determined by high-performance liquid chromatography (HPLC) using a C18 reverse-phase column (250 mm×4.6 mm, 5 μm), with a mobile phase of acetonitrile-water (60:40, v/v) at a flow rate of 1.0 mL/min, a detection wavelength of 254 nm, and a column temperature of 30 °C. The content of Cucurbitacin B in the supernatant was calculated by the standard curve method, and the loading rate was calculated according to Formula 1:

$$DLE(\%) = \frac{Encapsulated\ drug}{Total\ drug\ added} \times 100\% \quad (1)$$

For the drug release rate determination, 50 mg of the drug-loaded Dex-APDMS@CP1@1@Cucurbitacin B sample was placed in a dialysis bag with a molecular weight cutoff of 3500 Da, sealed, and placed in a conical flask containing 10 mL of release medium (pH 7.4 phosphate buffer solution (PBS) for mimicking physiological environment and pH 5.5 acetate buffer solution for mimicking tumor microenvironment). The conical flask was placed in a constant-temperature shaking water bath at 37 °C and 100 rpm. At time points of 0.5 h, 1 h, 2 h, 4 h, 6 h, 12 h, 24 h, 48 h, and 72 h, 1 mL of the release medium outside the dialysis bag was taken out, and 1 mL of fresh release medium was supplemented simultaneously. The taken samples were appropriately diluted, and the concentration of Cucurbitacin B was determined by HPLC. The content was calculated by the standard curve method, and the release rate was calculated according to the Formula 2:

$$DLC(\%) = \frac{Encapsulated\ drug}{Nanoparticle\ weight} \times 100\% \quad (2)$$

Determination of cell viability

The NSCLC cell line H1299 (ATCC, USA) was cultivated in Dulbecco's modified Eagle medium (DMEM; Gibco, USA) containing 10% fetal bovine serum (FBS; Gibco, USA) and subsequently seeded into a cell culture plate. Following a 48-hour treatment with cucurbitacin B-loaded nanoparticles (100nM), the cell activity was detected using a Cell Counting Kit-8 kit (CCK-8; Yeasen, China) according to the manufacturer's instructions, and the relative cell viability was calculated. The control cells were treated with Dex-APDMS@CP1@1.

Western blot

Following drug treatment, cells were lysed with RIPA lysis buffer (Beyotime, China). Proteins were separated by SDS-PAGE, transferred to a PVDF membrane and then blocked with skim milk. The membrane was then incubated with the primary antibody for 1h and the secondary antibody for 1h. Protein detection was performed using an ECL kit (Beyotime, China). The antibody information was follows, NLRP3 (1:1,000; Proteintech, China), GSDMD (1:1,000; Proteintech, China), IL-1β (1:1,000; Proteintech, China) and β-actin (1:20,000; Proteintech, China)

Statistical Analysis

All biological experiments were performed with n=3 independent replicates, and data are presented as "mean ± standard deviation (SD)", with standard deviations specified in the figure legends. For physicochemical experiments, each test was conducted in n=3 technical replicates. Statistical analyses were performed using Student's t-test or analysis of variance (ANOVA), with p-values indicated in the corresponding figures (e.g., $^{*}p<0.05$, $^{**}p<0.01$). The 95% confidence intervals (CIs) are included in the statistical reports.

RESULTS AND DISCUSSION

Description of the crystal structure for CP1

The crystal of CP**1** determined by the X-ray diffraction analysis crystallizes in the monoclinic system with $P2_1/c$ space group, showing a 1D ladder-like chain structure with the asymmetric unit containing one Cu(I) ion, a half L ligand as well as one CN^- anion. As shown in Fig. 1a, the Cu(I) ion is coordinated by two nitrogen atoms from one L ligand one CN^- anion, and one carbon atom from another CN^- anion. The Cu-N distances are in the range of 1.924(3)-2.170(2) Å and the Cu-C distance is

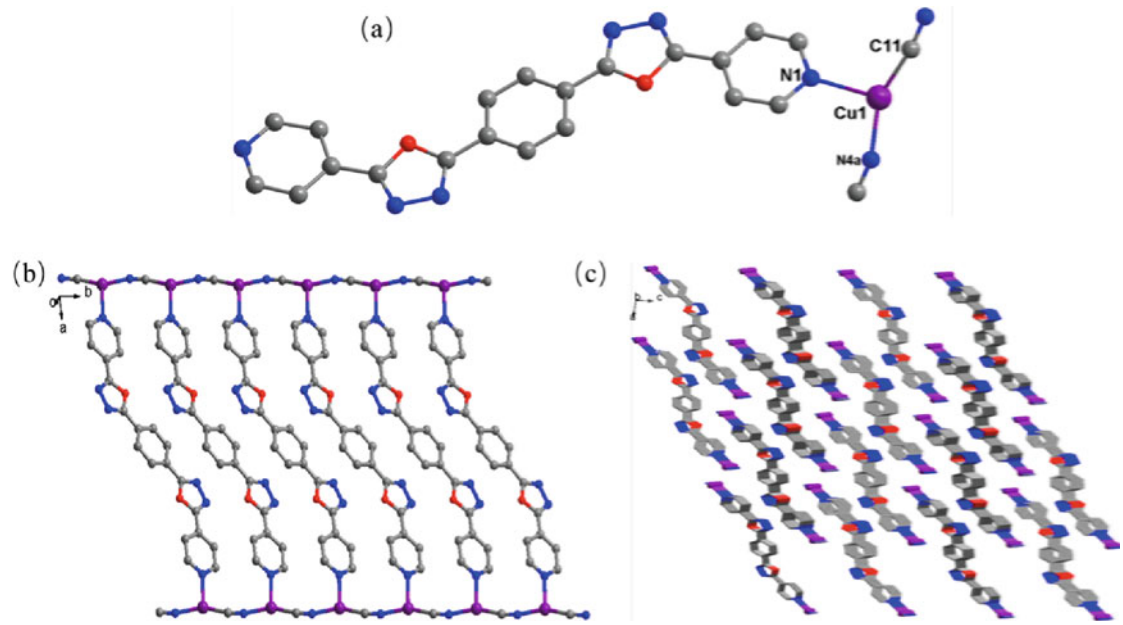

Figure 1. (a) Viewing of the coordination environments of Cu(II) ion in CP**1**. (b) The 1D ladder-like structure of 1. (c) The 3D stacked supramolecular framework of CP**1**

1.890(3) Å. Three bond angles around Cu(I) ion are 96.69(10)°, 109.41(10)°, 152.63(11)°, respectively, the sum of which is 358.73° which is nearly to 360°, indicating that the coordination geometry of Cu(I) ion is close to triangle. The L ligands in trans configuration and CN^- anions acting as linear bridges link all Cu(I) ions into a 1D ladder-like chain running along crystallographic *b* direction (Fig. 1b). By calculation using the PLATON program, there are no any hydrogen-bonding, π···π, C-H···π interactions between the adjacent 1D ladder-like chains. Thus, these 1D chains are finally stacked into a 3D supramolecular framework induced by the weak Van der Waals interactions (Fig. 1c).

Structure Description of Compound 1

The single crystal X-ray diffraction data of compound **1** show that compound **1** crystallizes with the monoclinic crystal system with the space group P2(1)/c. As shown in Fig. 2a, the molecule structure consists of two six-membered rings (ring A: C3-C4, C6, C11-C12 and N1, and ring B: C6-C11) and one benzene ring C: C13-C18. The atom C3 of ring A connects a methyl formate group ($C2H_5O_2C$-) via the bond of C2-C3. The C4 atom of the ring A connects to a methyl group (-$C5H_3$). Ring A and ring B connect to each other through the sharing of a C-C bond from C6 and C11. The atom C12 of ring A connects ring C via the C13 atom. The atom C10 of ring B connects to the O3 atom via a double bond of C=O. The C15 and C17 atoms of ring C connect to two fluoride ions, respectively. Furthermore, the neighbor-

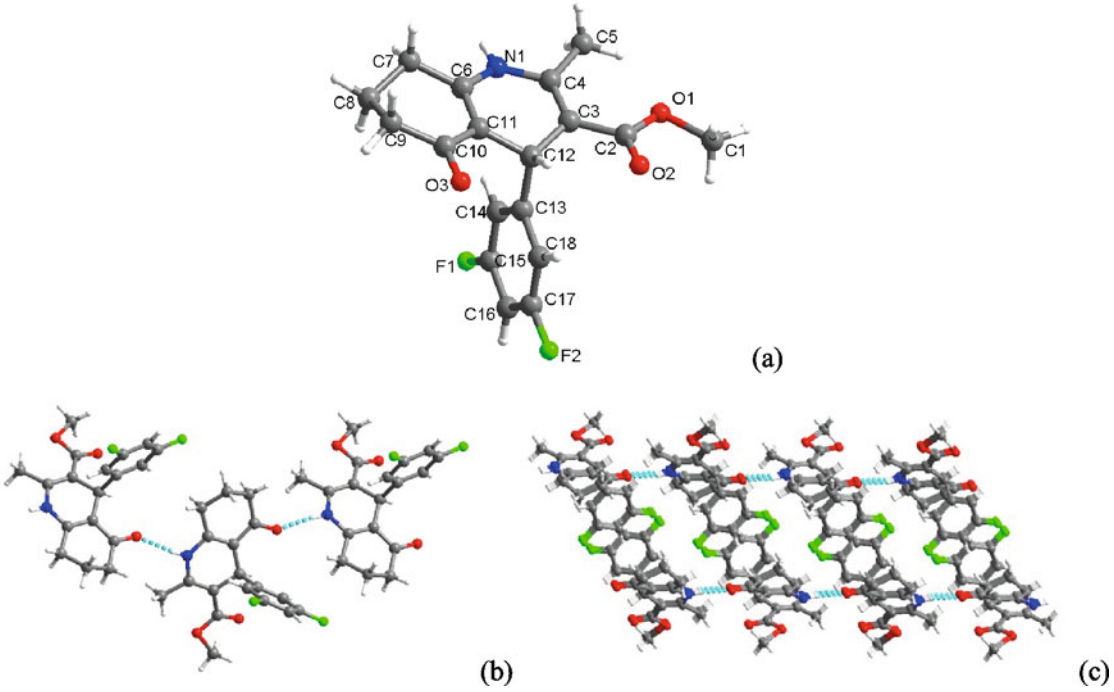

Figure 2. (a) The molecule structure for compound **1**; (b) The H-bonds between the adjacent molecules; (c) The dense packing molecule structure of compound **1**

ing molecules of compound **1** are further connected by intermolecular hydrogen bonds (O3-H1D…N1: 2.0074Å) (Fig. 2b) and van der Waals forces, which give a three-dimensional dense packing structure (Fig. 2c).

Structural characterization and Morphology

The successful synthesis and characterization of the fluorescent drug delivery system Dex-APDMS@CP1@1@Cucurbitacin B were confirmed using various analytical techniques. XRD analysis (Fig. 3a) revealed distinct crystalline peaks for the synthesized material, which aligned with the simulated diffraction pattern, validating the expected crystalline structure. SEM images (Fig. 3b) displayed a uniform particle size of approximately 500 nm, making it an ideal candidate for drug encapsulation and delivery. TGA (Fig. 3c) demonstrated excellent thermal stability, with a notable weight loss between 400–600 °C, indicating the presence of both drug and organic components, while confirming the material's thermal stability at lower temperatures. The nitrogen adsorption–desorption isotherms (Fig. 3d) demonstrate clear mesoporous behavior for both samples. Dex-APDMS@CP1 exhibits a higher nitrogen adsorption capacity, reaching approximately 180 cm^3/g STP at a relative pressure ($P/P_0 \approx 0.9$), indicating a well-developed porous structure. In contrast, the adsorption capacity of Dex-APDMS@CP1@1@Cucurbitacin B is notably reduced, suggesting that the pores were partially occupied or blocked following drug loading. This reduction in surface area and pore volume confirms the successful encapsulation of compound 1 and Cucurbitacin B, supporting the material's potential for drug delivery applications. Collectively, these findings demonstrate that Dex-APDMS@CP1@1@Cucurbitacin B is a robust and efficient drug delivery system with excellent stability, drug-loading capacity, and fluorescence properties, making it highly suitable for therapeutic applications.

Drug release study

The Dex-APDMS@CP1@1@Cucurbitacin B drug delivery system was thoroughly analyzed through various techniques, demonstrating its efficient drug encapsulation and controlled release. As shown in Fig. 4a, the uptake capacity of Dex-APDMS@CP1@1@Cucurbitacin B (red curve) increases rapidly within the first 20 hours, reaching equilibrium, while the Dex-APDMS@CP1@1 system (black curve) exhibits slower uptake, highlighting the enhanced absorption and encapsulation efficiency of Cucurbitacin B. Fig. 4b presents the Raman spectrum of the drug-loaded system, with significant peaks in the 100–240 cm^{-1} range, confirming the integration of Cucurbitacin B into the nanocarrier and the interaction between the drug and the polymer. The Raman spectrum of CP1@1@Cucurbitacin B in Fig. 4c, used as a baseline comparison, shows no polymer modification peaks, underscoring the impact of the Dex-APDMS modification. Finally, Fig. 4d presents the iodine release profile as a model for evaluating the drug release behavior of the nanocomposite. The red curve represents Dex-APDMS@CP1@1@Cucurbitacin B, which exhibits a remarkably fast release rate, reaching over 95% iodine release within the first 5 minutes and achieving nearly complete release (≈100%) within 10 minutes. This rapid burst release indicates efficient surface diffusion and enhanced release dynamics facilitated by the Dex and APDMS modification, which likely improve water penetration and accelerate diffusion. In contrast, the black curve, corresponding to CP1@1@Cucurbitacin B without Dex-APDMS functionalization, displays significantly slower kinetics. The release gradually increases over time, reaching approximately 85% after 120 minutes. The inset plot further highlights the sustained difference over an extended period, confirming that Dex-APDMS not only accelerates the release process but also impro-

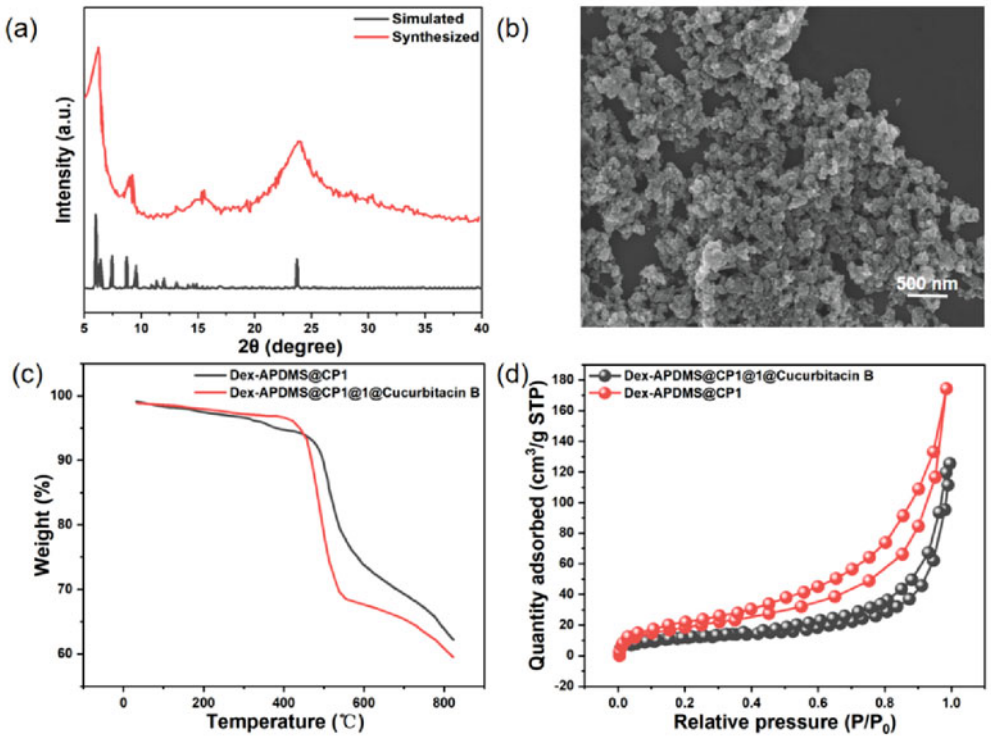

Figure 3. Characterization of Dex-APDMS@CP1@1@Cucurbitacin B. (a) XRD. (b) SEM. (c) TGA. (d) Nitrogen adsorption isotherms

ves total release efficiency. It is worth mentioning that the loading rate and release rate were 35.2 ± 2.1 wt % and 88.6 ± 3.5%, respectively. Fig. 4e displays the X-ray powder diffraction (XRD) patterns of Dex-APDMS@CP1 under different pH conditions (pH = 3, 5, 7, 9, and 11) to evaluate its structural stability. Distinct diffraction peaks are observed in the pH range of 3 to 9, indicating that the material maintains its crystalline structure over a wide range of acidic to neutral conditions. As the pH increases to 11, the diffraction peaks become significantly weaker and broader, with a notable attenuation of the main peak around 20°, suggesting partial degradation or disordering of the crystal structure under alkaline conditions. These results demonstrate that Dex-APDMS@CP1 exhibits good structural stability in neutral to mildly acidic environments, while some structural damage occurs under strongly alkaline conditions. Therefore, the material is expected to remain stable under physiological pH, meeting the basic structural requirements for drug delivery systems. These findings confirm the efficacy of the Dex-APDMS@CP1@1@Cucurbitacin B system in drug encapsulation, controlled release, and targeted delivery, making it a promising candidate for therapeutic applications.

Fluorescence performance testing

Furthermore, the fluorescence characteristics of Dex-APDMS@CP1 significantly change upon loading with Cucurbitacin B and compound 1. Fig. 5a shows the fluorescence emission spectra of the Dex-APDMS@CP1@Cucurbitacin B system at various concentrations of Cucurbitacin B (ranging from 0 to 35 μM). As the concentration of Cucurbitacin B increases, the fluorescence intensity decreases notably, indicating that drug loading results in fluorescence quenching. Fig. 5b illustrates the linear relationship between fluorescence intensity (I/I_0) and Cucurbitacin B concentration (0 to 35 μM), with a high correlation coefficient (R^2 = 0.9985) and binding constant ($K = 7.04 \times 10^5\ M^{-1}$), suggesting effective binding and significant fluorescence quenching. Fig. 5c demonstrates similar results for the Dex-APDMS@CP1@1 system at higher concentrations (0 to 250 μM). As the concentration increases, the fluorescence intensity continues to decrease, confirming the dose-dependent fluorescence reduction. Fig. 5d shows a linear relationship

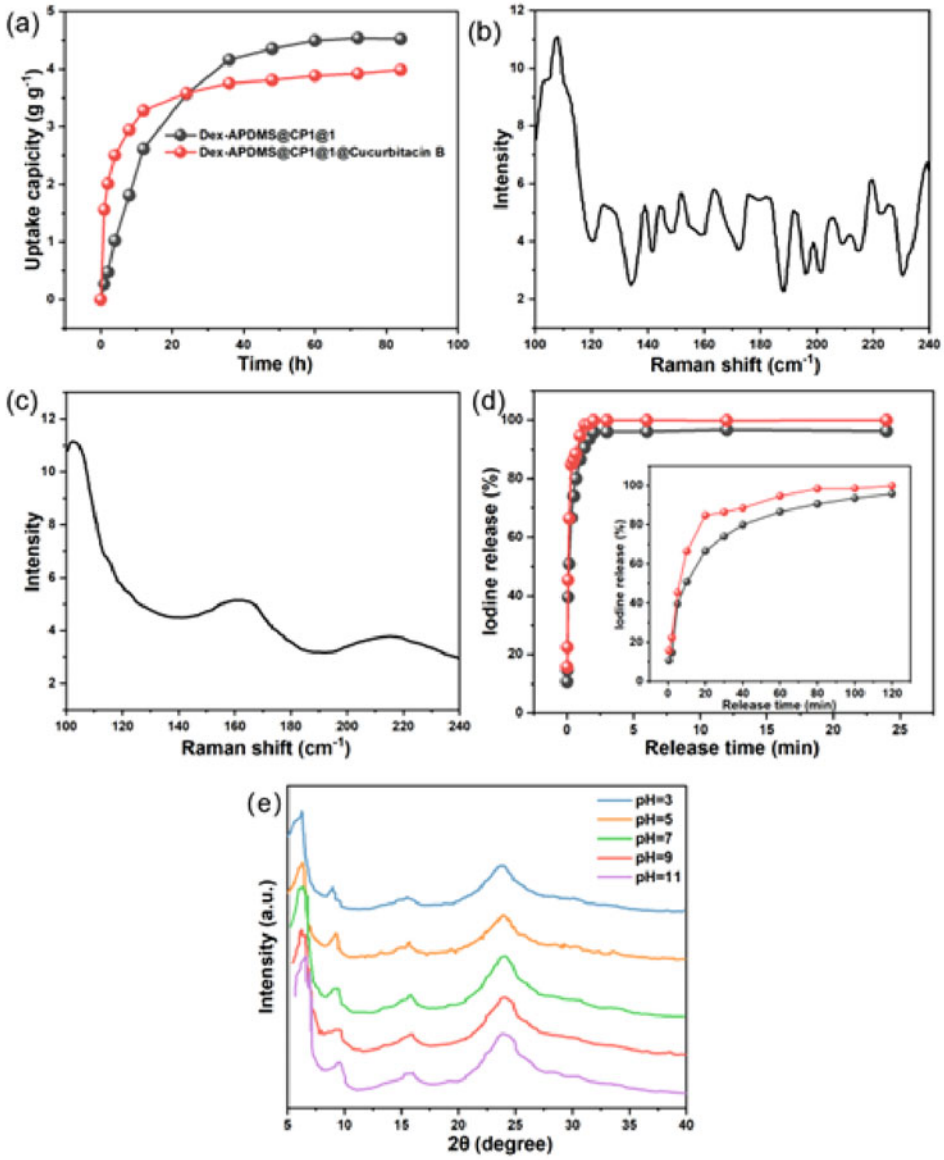

Figure 4. Dex-APDMS@CP1@1@Cucurbitacin B drug delivery system. (a) Uptake capacity of the drug-loaded system over time. (b) Raman spectrum of Dex-APDMS@CP1@1@Cucurbitacin B. (c) Raman spectrum of CP1@1@Cucurbitacin B, serving as a baseline comparison. (d) Cucurbitacin B release profile over time. (e) PXRD patterns at different pH

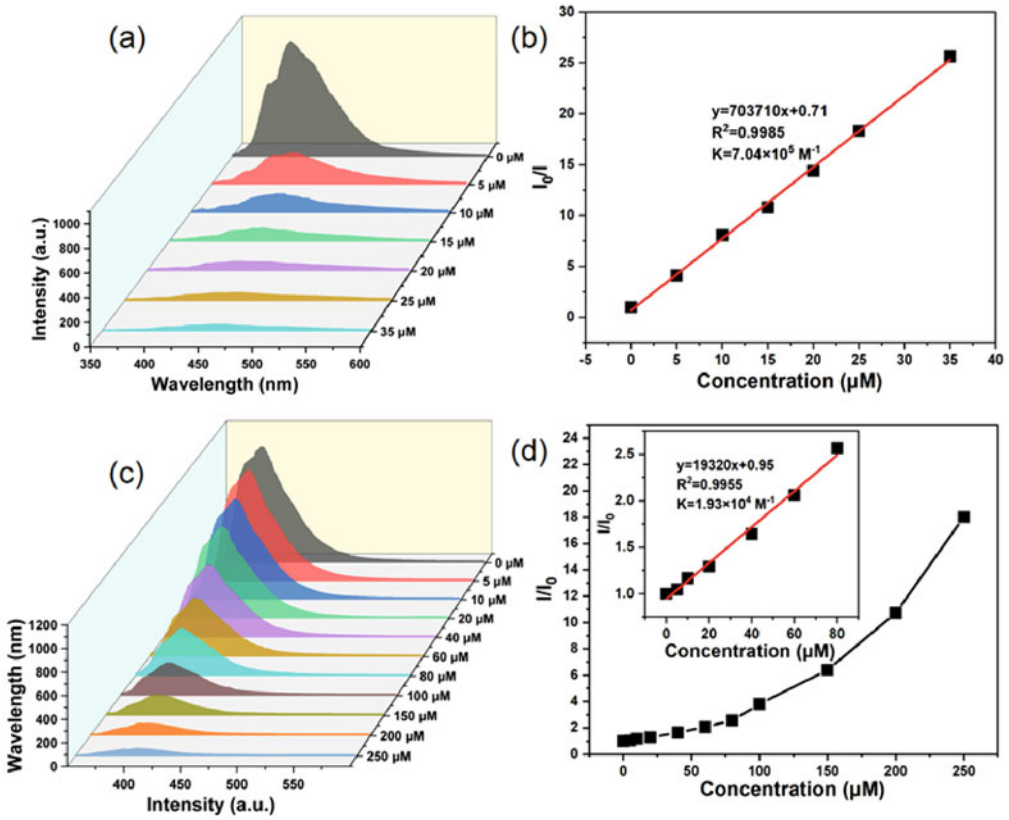

Figure 5. Fluorescence characteristics of Dex-APDMS@CP1 after loading with Cucurbitacin B and compound 1. (a) Fluorescence emission spectra of Dex-APDMS@CP1@Cucurbitacin B. (b) The linear relationship between fluorescence intensity (I/I_0) and Cucurbitacin B concentration. (c) Fluorescence emission spectra of Dex-APDMS@CP1@1 at higher concentrations (0 to 250 μM). (d) The linear relationship between fluorescence intensity and concentration for Dex-APDMS@CP1@1

between fluorescence intensity and concentration, with an R^2 value of 0.9955 and a binding constant ($K = 1.93 \times 10^4\ M^{-1}$), indicating the system's strong responsiveness to the loading of Cucurbitacin B. These results emphasize that the loading of Cucurbitacin B and compound 1 into the Dex-APDMS@CP1 system significantly alters its fluorescence properties, confirming the successful encapsulation of the drugs and demonstrating their potential for effective monitoring and targeted delivery in therapeutic applications.

Dex-APDMS@CP1@1@Cucurbitacin B induced pyroptosis to inhibit NSCLC proliferation

NSCLC cells were exposed to Dex-APDMS@CP1@1@Cucurbitacin B for 48 hours, and the alteration in cell viability was identified through the implementation of the CCK-8 assay. As illustrated in Fig. 6A, the cell activity exhibited a decline of 38% in the treatment group in comparison to the control group ($P<0.05$). Subsequently, we investigated whether the drug regulates pyroptosis in cells, and the expression of pyroptosis-related proteins was detected by western blot. Treatment of H1299 cells with Dex-APDMS@CP1@1@Cucurbitacin B resulted in a significant upregulation of NLRP3 and GSDMD proteins, as well as a substantial enhancement in the downstream expression of IL-1β (Fig. 6B). These findings suggest that Dex-APDMS@CP1@1@Cucurbitacin B induced pyroptosis and stimulated the inflammatory response in NSCLC cells. Additionally, to clearly highlight the advantages and distinctive features of our nanocarrier relative to other reported systems, we have included Table S1 in the Supporting Information, which compiles and compares the key parameters and performance metrics from representative recent studies.

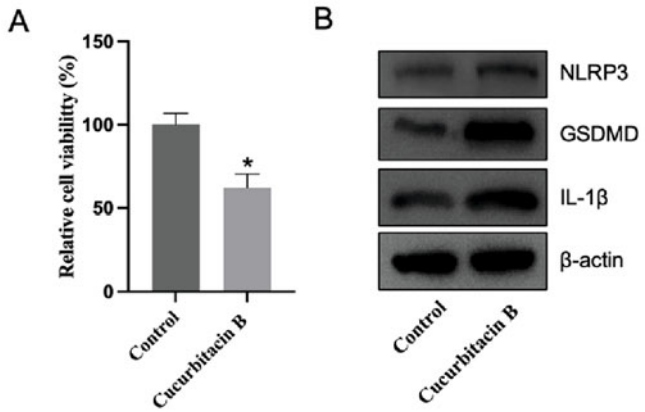

Figure 6. (A) The inhibitory effect of Dex-APDMS@CP1@1@Cucurbitacin B on NSCLC cell proliferation was assessed using CCK-8 assay. (B) The effect of Dex--APDMS@CP1@1@Cucurbitacin B on the expression of NLRP3, GSDMD and IL-1β was analyzed by western blot. *, $P < 0.05$

CONCLUSION

In conclusion, we have successfully synthesized and characterized the Dex-APDMS@CP1@1@Cucurbitacin B drug delivery system, which demonstrates substantial potential for cancer therapy. The system features excellent structural stability, efficient drug loading capacity, and sustained release performance, supported by its uniform particle size, thermal stability, high adsorption efficiency, and significant fluorescence quenching upon drug loading—all of which

underscore its suitability for targeted delivery applications. In vitro studies further validate its efficacy in inhibiting NSCLC cell proliferation, reinforcing its translational potential. Notably, while the current system showcases promising performance, limitations in long-term physiological stability, synthetic scalability, and comprehensive in vivo toxicity profiling are discussed in the Outlook section. These aspects highlight opportunities for optimization, positioning Dex-APDMS@CP1@1@Cucurbitacin B as a novel targeted delivery platform with significant potential to advance NSCLC therapeutic strategies.

DECLARATIONS

Ethical Approval

Not applicable.

Competing interests

The authors declare that no conflicts of interest exist in the distribution of this article.

Authors' contributions

Taixu Sun and Dengfeng Ge are responsible for conducting experiments in the chemical section; Ying Zhang is responsible for conducting experiments in the biology section; Bin Zhang wrote the paper.

Funding

The study was supported by "Study on Yifei Tongluo Decoction promoting rapid rehabilitation of patients with non-small cell lung cancer after operation" (Y2021ZR08).

Availability of data and materials

Supporting data derived from the results of this research are obtainable upon contact with the corresponding author.

LITERATURE CITED

1. Nie, W., Wang, Y., Tian, X., Liu, J., Jin, Z., Xu, J., He, M., Shen, Q., Guo, H. & Luan, T. (2024). Cucurbitacin B and Its Derivatives: A Review of Progress in Biological Activities. *Molecules* 29(17), 4193. DOI: 10.3390/molecules29174193.

2. Ge, W., Chen, X., Han, F., Liu, Z., Wang, T., Wang, M., Chen, Y., Ding, Y. & Zhang, Q. (2018). Synthesis of Cucurbitacin B Derivatives as Potential Anti-Hepatocellular Carcinoma Agents. *Molecules* 23(12), 3345. DOI: 10.3390/molecules23123345.

3. Tan, N., Li, Y., Ying, J. & Chen, W. (2024). Histological transformation in lung adenocarcinoma: Insights of mechanisms and therapeutic windows. *J. Transl. Int. Med*. 12(5), 452–465. DOI: 10.1515/jtim-2024-0019.

4. Zhang, H., Zhao, B., Wei, H., Zeng, H., Sheng, D. & Zhang, Y. (2022). Cucurbitacin B controls M2 macrophage polarization to suppresses metastasis via targeting JAK-2/STAT3 signalling pathway in colorectal cancer. *J. Ethnopharmacol.* 287, 114915. DOI: 10.1016/j.jep.2021.114915.

5. Li, Y., Yan, B. & He, S. (2023). Advances and challenges in the treatment of lung cancer. *Biomed. Pharmacother.* 169, 115891. DOI: 10.1016/j.biopha.2023.115891.

6. Tian, B., Pang, Y., Gao, Y., Meng, Q., Xin, L., Sun, C., Tang, X., Wang, Y., Li, Z., Lin, H. & Wang, L. (2023). A pan-cancer analysis of the oncogenic role of Golgi transport 1B in human tumors. *J. Transl. Int. Med.* 11(4), 433–448. DOI: 10.2478/jtim-2023-0002.

7. Turner, J., Pond, G.R., Tremblay, A., Johnston, M., Goss, G., Nicholas, G., Martel, S., Bhatia, R., Liu, G., Schmidt, H., Tammemagi, M.C., Puksa, S., Atkar-Khattra, S., Tsao, M.S., Lam, S. & Goffin, J.R. (2021). Risk Perception Among a Lung Cancer Screening Population. *Chest* 160(2), 718–730. DOI: 10.1016/j.chest.2021.02.050.

8. Traeger, R.S., Woodcock, J., Tan, S., Shi, Z. & Vasquez-Vivar, J. (2025). Tetrahydrobiopterin as a rheostat of cell resistance to oxidant injury. *Redox Biol*. 79, 103447. DOI: 10.1016/j.redox.2024.103447.

9. Luo, Z., Wan, R., Liu, S., Feng, X., Peng, Z., Wang, Q., Chen, S. & Shang, X. (2023). Mechanisms of exercise in the treatment of lung cancer–a mini-review. *Front. Immunol.* 14, 1244764. DOI: 10.3389/fimmu.2023.1244764.

10. Janssen, E.M., Smith, I.P., Liu, X., Pierce, A., Huang, Q., Kalsekar, I., Vachani, A. & Mansfield, C. (2023). Patient Preferences for Lung Cancer Interception Therapy. *JAMA Netw. Open* 6(11), e2342681. DOI: 10.1001/jamanetworkopen.2023.42681.

11. Bhattacharjee, J., Sarkar, A. & Panda, T.K. (2021). Recent development of alkali metal complex promoted iso-selective ring-opening polymerization of rac-Lactide. *Curr. Opin. Green Sust. 31*, 100545. DOI: 10.1016/j.cogsc.2021.100545.

12. Ahmad, M.G., Balamurali, M.M. & Chanda, K. (2023). Click-derived multifunctional metal complexes for diverse applications. *Chem. Soc. Rev.* 52(15), 5051–5087. DOI: 10.1039/d3cs00343d.

13. Chen, L.J., Zhao, X., Liu, Y.Y. & Yan, X.P. (2020). Macrophage membrane coated persistent luminescence nanoparticle@MOF-derived mesoporous carbon core–shell nanocomposites for autofluorescence-free imaging-guided chemotherapy. *J. Mater. Chem. B* 8(35), 8071–8083. DOI: 10.1039/d0tb01272f.

14. Sun, X., He, G., Xiong, C., Wang, C., Lian, X., Hu, L., Li, Z., Dalgarno, S.J., Yang, Y.W. & Tian, J. (2021). One-Pot Fabrication of Hollow Porphyrinic MOF Nanoparticles with Ultrahigh Drug Loading toward Controlled Delivery and Synergistic Cancer Therapy. *ACS Appl. Mater. Interfaces* 13(3), 3679–3693. DOI: 10.1021/acsami.0c20617.

15. Das, B. & Gupta, P. (2024). Multimetallic transition metal complexes: Luminescent probes for biomolecule sensing, ion detection, imaging and therapeutic application. *Coord. Chem. Rev.* 504, 215656. DOI: 10.1016/j.ccr.2024.215656.

16. Gaikwad, D., Sutar, R. & Patil, D. (2024). Polysaccharide mediated nanodrug delivery: A review. *Int. J. Biol. Macromol.* 261(1), 129547. DOI: 10.1016/j.ijbiomac.2024.129547.

17. Srivastav, A.K., Rajput, P.K., Jaiswal, J., Yadav, U.C.S. & Kumar, U. (2024). In vitro and in silico investigation of glycyrrhizic acid encapsulated zein nanoparticles: A synergistic targeted drug delivery approach for breast cancer. *Int. J. Biol. Macromol.* 266(2), 131368. DOI: 10.1016/j.ijbiomac.2024.131368.

18. Zhao, C., Pan, B., Wang, T., Yang, H., Vance, D., Li, X., Zhao, H., Hu, X., Yang, T., Chen, Z., Hao, L., Liu, T. & Wang, Y. (2023). Advances in NIR-Responsive Natural Macromolecular Hydrogel Assembly Drugs for Cancer Treatment. Pharmaceutics 15(12), 2729. DOI: 10.3390/pharmaceutics15122729.

19. Korpi, A., Anaya-Plaza, E., Välimäki, S. & Kostiainen, M. (2020). Highly ordered protein cage assemblies: A toolkit for new materials. *WIREs Nanomed. Nanobiotechnol.* 12(1), e1578. DOI: 10.1002/wnan.1578.

20. Pauli, F.P., Freitas, C.S., Pereira, P.R., Magalhães, A., De Carvalho Da Silva, F., Paschoalin, V.M.F. & Ferreira, V.F. (2023). Exploring the Antimicrobial and Antitumoral Activities of Naphthoquinone-Grafted Chitosans. *Polymers* 15(6), 1430. DOI: 10.3390/polym15061430.

21. Li, D.Q., Li, J., Dong, H.L., Li, X., Zhang, J.Q., Ramaswamy, S. & Xu, F. (2021). Pectin in biomedical and drug delivery applications: A review. *Int. J. Biol. Macromol. 185*, 49–65. DOI: 10.1016/j.ijbiomac.2021.06.088.

22. Kong, W.Q., Gao, C.D., Hu, S.F., Ren, J.L., Zhao, L.H. & Sun, R.C. (2017). Xylan-Modified-Based Hydrogels with Temperature/pH Dual Sensitivity and Controllable Drug Delivery Behavior. *Materials* 10(3), 304. DOI: 10.3390/ma10030304.

23. Agnes, M., Mazza, A., Malanga, M., Manet, I. (2024). Sculpturing the future of water-soluble cyclodextrin branched polymers in pharmaceutical applications. *J. Mater. Chem. B* 12(33), 7969–7976. DOI: 10.1039/d4tb01165a.

24. Joyce, K., Fabra, G.T., Bozkurt, Y., Pandit, A. (2021). Bioactive potential of natural biomaterials: identification, retention and assessment of biological properties. *Signal Transduct. Tar.* 6(1), 122. DOI: 10.1038/s41392-021-00512-8.